Volume 1 | Number 1 | Jan 2013 | Pages 1–100

Journal of
Materials Chemistry A

Materials for energy and sustainability
www.rsc.org/materialsA

Li⁺

ROYAL SOCIETY
OF CHEMISTRY

ROYAL SOCIETY
OF CHEMISTRY

www.rsc.org/materialsA

Migration Mechanism of Transition Metal Ions in LiNi$_{0.5}$Mn$_{1.5}$O$_4$

Guiliang Xu[a], Yan Qin[a], Yang Ren[b], Lu Cai[c], Ke An[c], Khalil Amine[a], and Zonghai Chen[a]*

a)   *Chemical Sciences and Engineering Division, Argonne National Laboratory, 9700 South Cass Avenue, Lemont, IL 60439, USA*

b)   *X-ray Science Division, Argonne National Laboratory, 9700 South Cass Avenue, Lemont, IL 60439, USA*

c)   *Chemical and Engineering Materials Division, Spallation Neutron Source, Oak Ridge National Laboratory, 1 Bethel Valley Rd, Oak Ridge, TN 37831, USA*

*Corresponding author: zonghai.chen@anl.gov

Abstract

The migration of transition metal ions in the oxygen framework was recently proposed to be responsible for the continuous loss of average working potential of high energy density layered-layered composite cathodes for lithium-ion batteries. The potential migration pathway in a model material, LiNi$_{0.5}$Mn$_{1.5}$O$_4$ spinel, was investigated using *in situ* high-energy X-ray diffraction and *in situ* neutron diffraction during the solid state synthesis process. It was found that the migration of transition metal ions among octahedral cites is possible by using tetrahedral vacancies as intermediate sites. It was also suggested that the number of electrons in 3d orbitals has significant impact on their mobility in the hosting oxygen framework.

Keywords: cation migration, lithium transition metal oxide, cathode, lithium-ion battery

1

Introduction

Lithium transition metal oxides are dominant cathode materials for lithium-ion batteries that power the modern portable electronics, and as well as emerging hybrid electric vehicles and electric vehicles.[1-3] The research effort to understand the structural stability and the mobility of cations in this class of materials has been dramatically boosted due to their emerging application for the electrification of the transportation system.[4-14] In lithium transition metal oxides, the oxygen atoms generally adopt a face centered cubic (FCC) structure, forming the supporting framework to host lithium ions and transition metal ions in its octahedral sites and/or tetrahedral sites.[15-17] Different type of materials, ranging from rock salt structure,[17-20] to spinel[16, 21-28] and classical layered structure,[29, 30] can be formed by filling vacancies with different ratio of cations with different filling patterns. Layered $LiMO_2$ crystallize in the α-$NaFeO_2$ structure can be viewed as "ordered rock-salt" in which alternate layers of lithium ions and transition metal ions occupy in the octahedral sites within the cubic close packed oxygen array, while in the case of spinel cathode; lithium ions occupy in the tetrahedral *8a* sites, transition metal ions occupy in the octahedral *16d* sites and the oxygen ions occupy the *32e* sites arranged in an almost cubic close-packed manner. It's obvious that the essential difference between layered cathode and spinel cathode is that lithium ions occupy in the octahedral sites and tetrahedral sites, respectively. It should be also pointed out that the migration path in layered and spinel cathode are also different, the transition metal ions may migrate to lithium layer first and then migrate along the lithium layer, while no such lithium layer exist in the spinel cathode. The common feature of this class of materials is that their lithium ions are mobile in the oxygen framework while the transition metal ion has

extremely low or no mobility in the framework, offering the desired reversible charge storage mechanism for long-life and high energy-density lithium-ion batteries.

The recent development effort on layered-layered composite lithium transition metal oxides as potential high energy-density cathode materials has brought the mobility of transition metal ions into the spotted light.[7, 8, 29, 30] Among reported cathode materials, layered-layered composite cathodes have been reported to have the highest initial energy density when the materials are charged/discharged within a wide potential window, like between 2.0 V and 4.6 V.[31-39] However, the major barrier for this class of materials is the continuous loss of their average working potential during the normal operation,[6, 10, 12, 13, 40, 41] which phenomenon is also defined as the voltage fade. The loss of the average working potential will not only lead to a substantial loss of effective energy density of the battery, but also raise an unexpected challenge for the battery management system. Recent intensive investigation on the structural stability of layered-layered composite cathodes has led to a speculation that the migration of transition metal ions in the oxygen framework is the fundamental cause of the voltage fade.[11-14, 32] However, the unresolved issue for this hypothesis is the selective importance of the migration of transition metal ions in layered-layered composite cathodes, although they share the same oxygen framework with other type of layered materials which have no reported issue on voltage fade.[1, 26, 42] Therefore, a clear understanding on the migration mechanism of transition metal ions is critical to tackle the above challenge and to shed light on potential solution for layered-layered composite cathodes.

Since layered-layered composite cathodes share the same oxygen framework with other type of oxides, $LiNi_{0.5}Mn_{1.5}O_4$ was selected as the model material to simplify the

investigation. In this work, both *in situ* high-energy X-ray diffraction (HEXRD) and *in situ* neutron diffraction (ND) were deployed to trace the migration of transition metal ions during the solid state synthesis of $LiNi_{0.5}Mn_{1.5}O_4$ spinel, and the mechanism of the cation migration is also proposed.

Experimental

Preparation of $Ni_{0.25}Mn_{0.75}CO_3$ precursor – $Ni_{0.25}Mn_{0.75}CO_3$ precursor was prepared through a co-precipitation process in a continuously stirred tank reactor according to the previous reported work.[43] In a typical synthesis, a 2 M acid solution consist of $NiSO_4$ (99.0%, Aldrich) and $MnSO_4$ (≥99.0%, Aldrich) (Ni: Mn =1:3 molar ratio), and a 2M basic solution of Na_2CO_3 (≥99.5%, Aldrich) with 0.2 M NH_4OH as a chelating agent were prepared respectively. The co-precipitation temperature was set at 60 °C, and the pH value was adjusted to 8.0. When the acidic and basic solutions were pumped to the reactor, particles were immediately formed. The resulting $Ni_{0.25}Mn_{0.75}CO_3$ powder was then collected by washing with deionized water for several times, and dried inside a vacuum oven at 120 °C for 12 hours.

In situ **HEXRD** – The as-prepared $Ni_{0.25}Mn_{0.75}CO_3$ precursor was mixed with Li_2CO_3 with a molar ratio of 4:1 using a rotatory mixer. After mixing, the mixture was pressed into pellets about 2 mm in thickness. The pellet was then placed vertically in a programmable furnace with glass windows. The sample was heated up to 800 °C with a heating rate of 1 °C min^{-1}. The in situ HEXRD experiment was carried out at the sector 11 of Advanced Photon Source (APS) of Argonne National Laboratory, the wavelength of X-ray used was pre-set to 0.107805 Å.[44] The high energy X-ray source was selected for its excellent penetration capability to detect structural changes on bulk part of the

sample. During the course of solid state synthesis, a high energy X-ray hit the sample horizontally, and a 2D X-ray detector was used to collect the X-ray diffraction (XRD) profiles using a transmission mode with a speed of one spectrum per minute.

***In situ* Neutron Diffraction –** The *in situ* neutron diffraction experiment was carried out at VULCAN of Spallation Neutron Source of Oak Ridge National Laboratory.[45] The mixture of $Ni_{0.25}Mn_{0.75}CO_3$ and Li_2CO_3 were pressed into 5-6 mm pellets, and the pellets were stacked in a tube furnace for the *in situ* neutron diffraction experiment. The furnace was heated to specified temperature at a heating rate of 5 °C min^{-1} and held the temperature for 3 hours for the collection of neutron diffraction data. The data was collected at 300, 400, 500, 600, 700, 800 and 900 °C, respectively.

Covariance analysis of *in situ* HEXRD data - The covariance analysis (see Equation 1) was applied to calculate the mathematical similarity between two different XRD patterns (*r1* and *r2*), both of which are a series of X-ray intensity at different 2θ values. When two spectra are identical to each other, the covariance value of Equation 1 equals to 1; a smaller number will be given when two spectra have some difference.

$$CORR(r1,r2) = \frac{\sum_i r1(i) * r2(i)}{\sqrt{\sum_i r1(i)*r1(i)} * \sqrt{\sum_i r2(i)*r2(i)}} \qquad \text{Equation 1}$$

Results

Figure 1 HEXRD pattern of the starting material.

Figure 1 shows the HEXRD pattern of the starting material, a mixture of $Ni_{0.25}Mn_{0.75}CO_3$ and Li_2CO_3 with the molar ratio of 4:1. All the diffraction peaks can be well assigned to Li_2CO_3 (C2/c, space group #15) with a=8.34455(9) Å, b=4.96689(9) Å and c=6.19395(6) Å and $MnCO_3$ ($R\bar{3}C$, space group #167) with a=b=4.77343(1) Å and c=15.51028(5) Å, presuming that HEXRD has limited contrast between Ni and Mn.
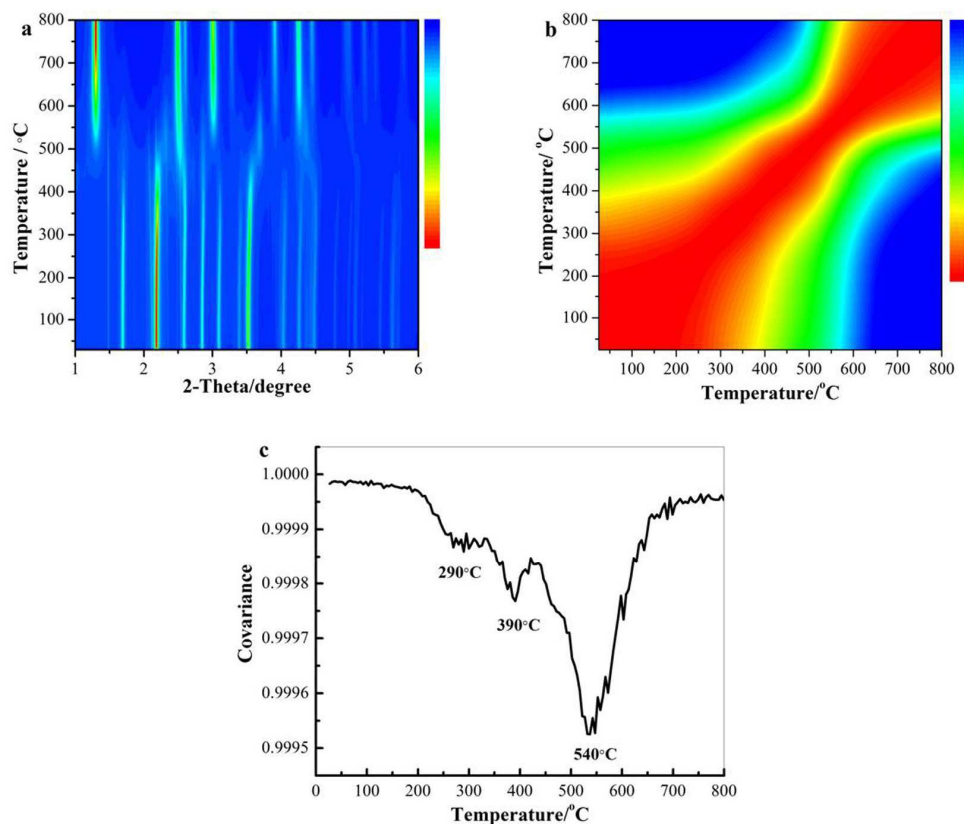
Figure 2 (a) A contour plot of HEXRD patterns collected during the solid state synthesis, (b) 2D and (c) 1D covariance analysis of adjunct HEXRD patterns.

Figure 2a shows a contour plot of *in situ* HEXRD patterns illustrating the structural evolution of the material during the heating process from the room temperature to 800 ^{o}C with a constant heating rate of 1 ^{o}C min^{-1}. Figure 2a clearly shows that a major reaction occurred at about 500 ^{o}C; the diffraction peaks from the starting material completely disappeared and a set of new peaks for the final product emerged. In order to trace subtle changes that are not visually clear in Figure 2a, 2D covariance analysis was carried out to obtain a mathematical description on the change of HEXRD patterns as shown in Figure 2b. Note that a red color means a high covariance value of 1, meaning no change was observed; while a blue color means a rapid change on HEXRD the pattern was observed. The 2D covariance analysis suggests two major reactions occurred at about 400 ^{o}C and

540 ^{o}C, indicated by the necking of the red spear-shape zone. For a clearer illustration, the 1D covariance analysis of adjunct HEXRD patterns, in real time space, is plotted in Figure 2c. In Figure 2c, three downward peaks at about 290 ^{o}C, 390 ^{o}C, and 540 ^{o}C suggest that three different reactions occur at the specific temperatures.
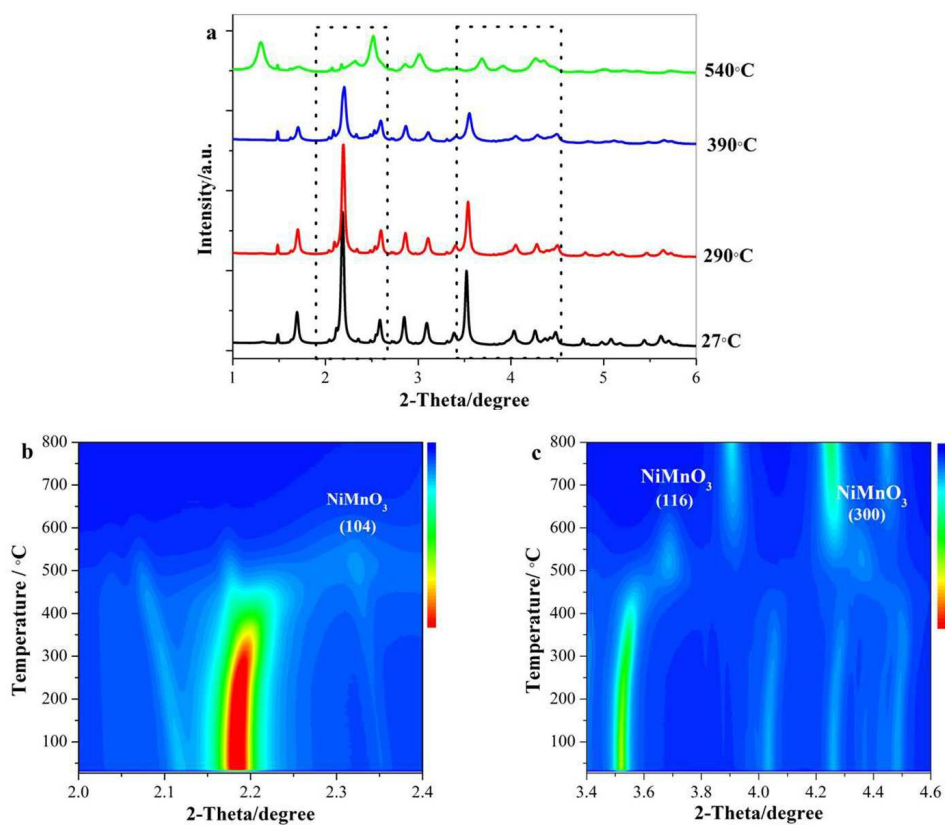

Figure 3 (a) HEXRD patterns collected at various temperatures and contour plot of HEXRD patterns with a 2θ region of (b) 2.0-2.4^{o} and (c) 3.4-4.6^{o} during the solid state synthesis.

Figure 3a compares the HEXRD patterns collected at 27 ^{o}C, 290 ^{o}C, 390 ^{o}C and 540 ^{o}C respectively. The HEXRD pattern collected at 540 ^{o}C is substantially different from those collected at lower temperatures, clearly suggesting the formation of a new structure that will be later determined to be LiNi$_{0.5}$Mn$_{1.5}$O$_{4}$. While the three patterns collected at lower temperatures look very similar except that their peak intensity

decreased with increase of the temperature. It's a common sense that the lattice of crystal will expand upon heating, and that all diffraction peaks will shift towards lower 2θ values. In contrast, the major peaks of the starting material consistently move towards higher 2θ values with increasing the temperature (Figures 3b and 3c). Deng et al. has previously shown that $Ni_{0.25}Mn_{0.75}CO_3$ started to decompose at about 200 ^{o}C from the TGA analysis of $Ni_{0.25}Mn_{0.75}CO_3$, and a mixed oxide composed of two stable phases, $NiMnO_3$ and Mn_2O_3 was formed after completion of this process at about 600 ^{o}C as indicated by equation 2.[43] In our case, when the heating temperature reached above 240 ^{o}C, the peak at about 2.175^{o} that is assigned to $Ni_{025}Mn_{0.75}CO_3$ and Li_2CO_3 kept decreasing the intensity and moving towards higher 2θ values (Figure 3b and Figure S1a), indicating that $Mn_{0.75}Ni_{0.25}CO_3$ was continuously decomposed noted that Li_2CO_3 start to decompose at about 500 ^{o}C, and a new phase assigned to be Mn_2O_3 ($R\bar{3}C$, space group #167) was formed. Figure 3b shows that a small peak at about 2.18^{o} that is assigned to be MnO_2 (PDF#12-0141) appeared at about 420 ^{o}C (Figure S1b), which is ascribe to the transformation from Mn_2O_3 to MnO_2 (Equation 3). When the temperature reached about 500 ^{o}C, the XRD peak of Mn_2O_3 could be hardly seen (Figure S1b), and the intensity of peaks for MnO_2 started to decrease simultaneously owing to not more conversion of Mn_2O_3 to MnO_2 and gradual conversion of MnO_2 into other phase. Figure 3b and 3c clearly shows the formation and consumption of a crystalline intermediate phase at about 450 ^{o}C and 500 ^{o}C, respectively (three small island at about 2.35^{o}, 3.68^{o} and 4.32^{o}), which can be well indexed as (104), (116) and (300) of $NiMnO_3$ (PDF#12-0269). Actually, $NiMnO_3$ might form upon the decomposition of $Ni_{0.25}Mn_{0.75}CO_3$ at above 240 ^{o}C, however, the crystalline peaks of $NiMnO_3$ emerged at a temperature as high as 450 ^{o}C,

which might be due to the amorphous state of $NiMnO_3$ particles at relatively lower temperatures. With the consumption of $NiMnO_3$, $LiNi_{0.5}Mn_{1.5}O_4$ started to form as can be seen in the Figure S1c (Equation 4). Therefore, the formation mechanism of $LiNi_{0.5}Mn_{1.5}O_4$ from Li_2CO_3 and $Ni_{0.25}Mn_{0.75}CO_3$ could be concluded as follows (Equation 2-4):

$$4Ni_{0.25}Mn_{0.75}CO_3 + O_2 \longrightarrow NiMnO_3 + Mn_2O_3 + 4CO_2 \;(240°C\text{-}500°C) \qquad \text{Equation 2}$$

$$2Mn_2O_3 + O_2 \longrightarrow 4MnO_2 \;(420°C\text{-}500°C) \qquad \text{Equation 3}$$

$$Li_2CO_3 + 2MnO_2 + NiMnO_3 \longrightarrow 2LiNi_{0.5}Mn_{1.5}O_4 + CO_2 \;(500°C) \qquad \text{Equation 4}$$
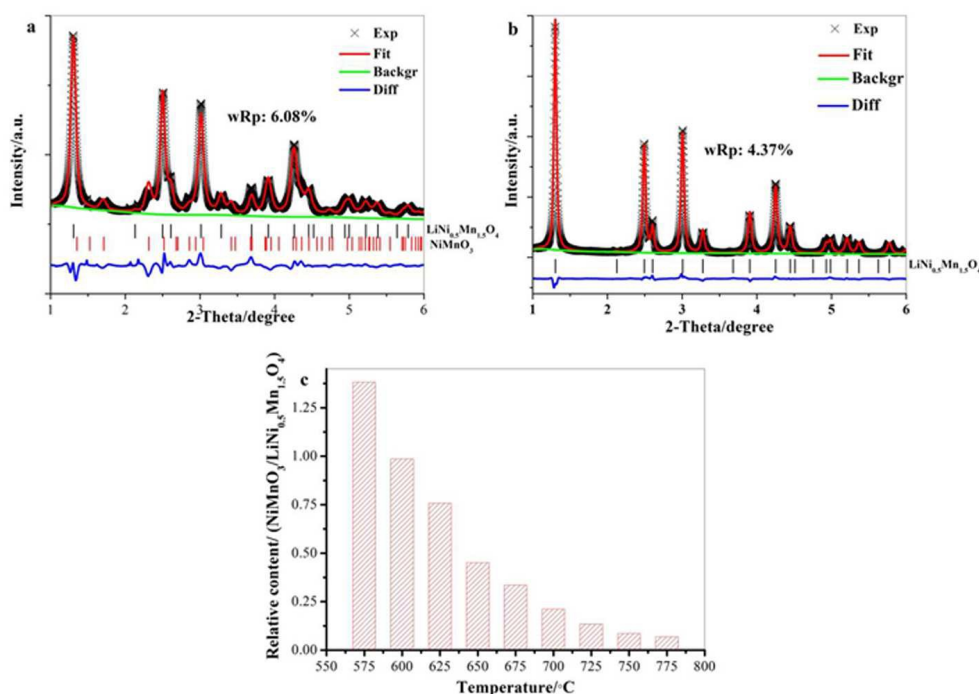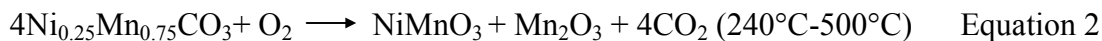

Figure 4 Rietveld refinement for HEXRD data collected at (a) 600 °C and (b) 800 °C and (c) the relative content of $NiMnO_3/LiNi_{0.5}Mn_{1.5}O_4$ as a function of the temperature.

Figure 2a shows that the final material emerged when the temperature was above 500 °C. Hence, Rietveld refinement was carried out to fit HEXRD profiles collected at temperatures above 575 °C. Figures 4a and 4b shows two typical results of Rietveld

refinement for data collected at 600 $^{\circ}$C and 800 $^{\circ}$C, respectively. Figure 4a shows two model structures, NiMnO$_3$ (PDF#12-0269) and disordered LiMn$_{1.5}$Ni$_{0.5}$O$_4$ (Fd$\bar{3}$m, space group #227), were needed to fit the experimental data collected at 600 $^{\circ}$C. The relative content between NiMnO$_3$ and LiMn$_{1.5}$Ni$_{0.5}$O$_4$ as a function of experimental temperature is shown in Figure 4c, which illustrates that the content of NiMnO$_3$ intermediate steadily decreased with the heating process owing to the gradual conversion of NiMnO$_3$ to LiNi$_{0.5}$Mn$_{1.5}$O$_4$, and almost no significant amount of NiMnO$_3$ was detected by HEXRD at 800 $^{\circ}$C. However, no clear evidence of transition metal ion migration could be obtained here due to the lack of contrast between Ni and Mn by HEXRD. Hence, *in situ* Neutron diffraction was then carried out to investigate the possible migration mechanism of transition metal ions.
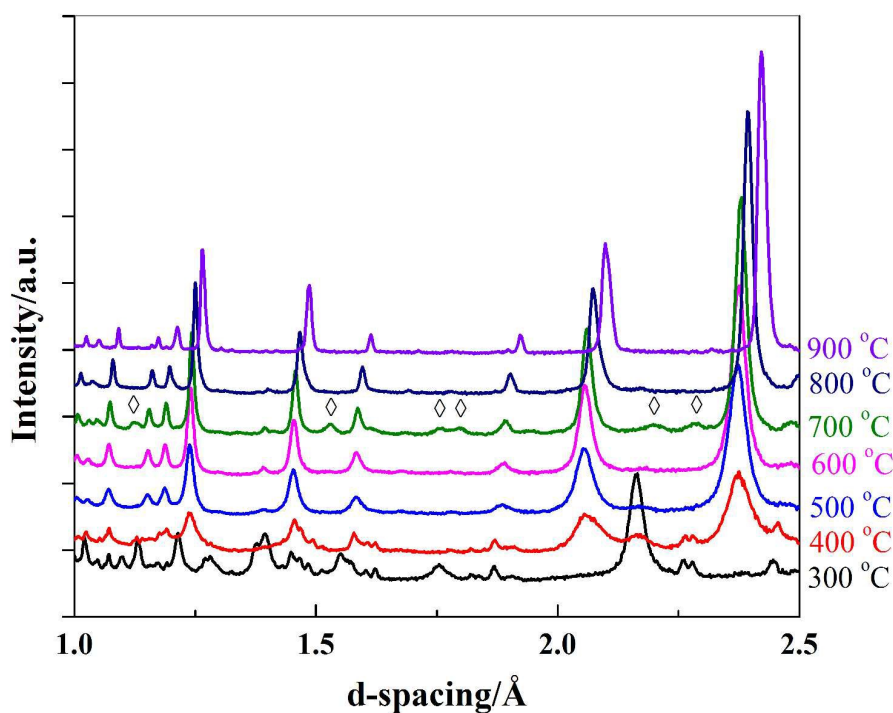

Figure 5 Neutron diffraction profiles collected at various temperatures during solid state synthesis. The peaks marked by diamonds are ascribed to ordered LiNi$_{0.5}$Mn$_{1.5}$O$_4$ spinel.

Figure 5 shows neutron diffraction profiles collected during the *in situ* solid state synthesis of LiNi$_{0.5}$Mn$_{1.5}$O$_4$ at various temperatures. The furnace was held at specific temperatures for 3 hours to collect a complete neutron diffraction profile. Figure 5 shows that the disordered LiMn$_{1.5}$Ni$_{0.5}$O$_4$ spinel (Fd$\bar{3}$m, space group #227) was formed at about 500 ^{o}C. This observation agreed well with the *in situ* HEXED experiment. When the temperature was increased to 700 ^{o}C, a set of new peaks, labeled by diamonds in Figure 5, were observed, and those peaks disappeared again when the temperature was increased to 800 ^{o}C and above.[46] Rietveld refinement analysis indicated that the extra peak for the profile collected at 700 ^{o}C belonged to the ordered LiNi$_{0.5}$Mn$_{1.5}$O$_4$ spinel (P$_4$332, space group #212). In the disordered spinel, Ni ions and Mn ions randomly occupied 50% of octahedral sites in the FCC oxygen framework without forming a long term ordering between Ni and Mn. On the other hand, in the ordered spinel, one Ni ion pairs with three Mn ions to form a stable repeating unit in the FCC oxygen framework, resulting in extra peaks in the neutron diffraction profile.[47, 48] Figure 6 shows a good fit towards the neutron diffraction data using a combination of an ordered spinel and a disordered spinel. The fitting results reveal that the relative content of the ordered spinel peaked at about 700 ^{o}C (Figure 7). Figure 7 also implies that the ordered spinel is energetically more stable than the disordered spinel. The phase transformation from the ordered spinel to the disordered spinel at high temperature (>700 ^{o}C) was primarily driven by the entropy, which tends to maximize the randomness of the system. The dominant presence of the disordered spinel at 500 ^{o}C and 600 ^{o}C can probably originated from the random distribution of Ni and Mn in the co-precipitated precursor of Ni$_{0.25}$Mn$_{0.75}$CO$_3$, presuming that the mobility of transition metal ions are very low at a

relative low temperature. In other word, the migration of transition metal ions was only enabled at a temperature around 700 ^{o}C to allow for the transformation of the metastable disordered spinel into a stable ordered spinel at about 700 ^{o}C.
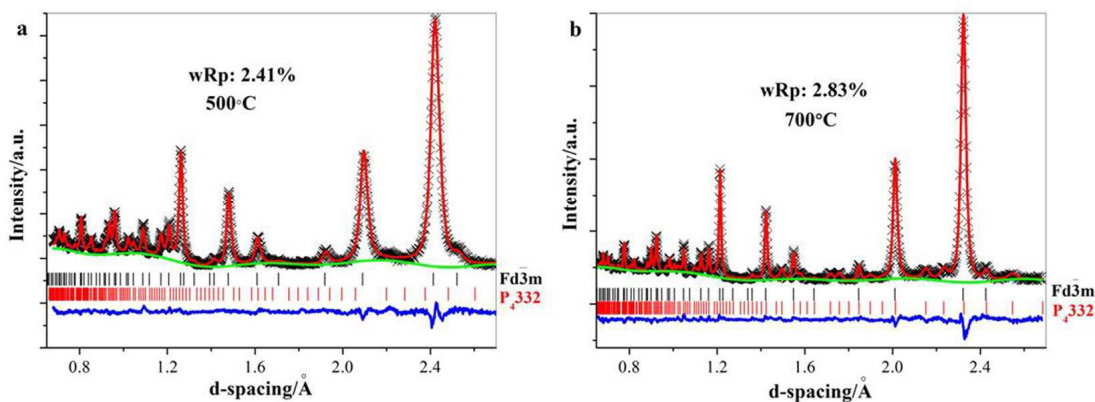

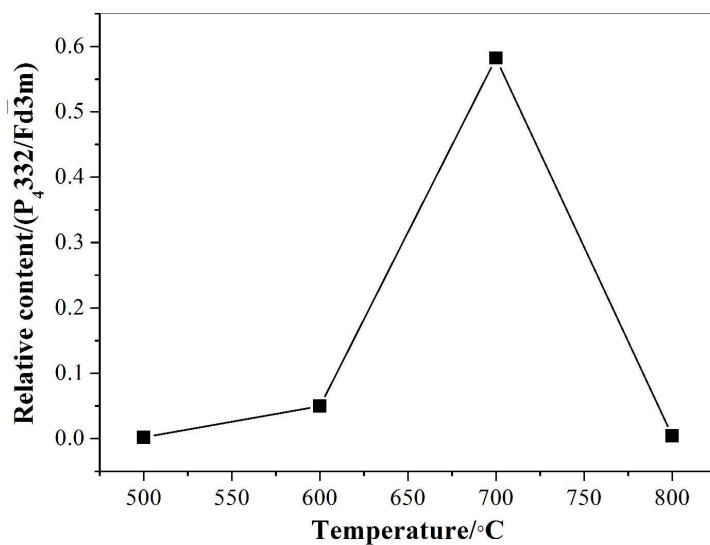Figure 6 Rietveld refinement of neutron diffraction profiles collected at (a) 500 ^{o}C and (b) 700 ^{o}C.

Figure 7 Relative content of ordered/disordered $LiNi_{0.5}Mn_{1.5}O_4$ as a function of the temperature obtained from for neutron scatting profiles collected at various temperatures during the solid state synthesis.
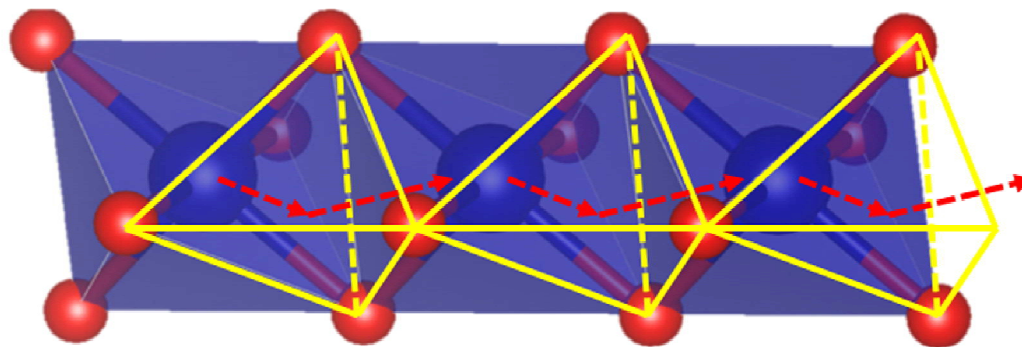
Discussion

Figure 8 Schematics showing the migration pathway of transition metal ions between the octahedra sites and tetrahedral sites.

The mobility of transition metal ions in the oxygen framework has been theoretically predicted and experimentally confirmed during the charge/discharge of cycling of layered-layered composite oxides at the room temperature.[9, 12, 49, 50] However, it was found here that the mobility of Ni and Mn was observed at a fairly high temperature (>600 °C). This discrepancy might be originated from one or more of following factors: (1) difference on the availability of adjunct vacancies for cations to migrate, (2) difference in the size of cations; and (3) the difference of the spin state of cations.

First of all, the availability of adjunct vacancies shouldn't be the dominant factor that leads to the low mobility of transition metal ions in $LiNi_{0.5}Mn_{1.5}O_4$. In layered-layered composite oxides, all octahedral sites are fully occupied by cations (about 50% by lithium ions and about 50% by transition metal ions).[50] Even when the layered-layered composite oxides were charged to a very high potential to remove most of lithium, leading to roughly 50% of octahedral vacancy in the oxygen framework. In $LiNi_{0.5}Mn_{1.5}O_4$, only 50% of octahedral sites are occupied by transition metal ions, and lithium ions occupy 25% of tetrahedral sites.[50] In other word, $LiNi_{0.5}Mn_{1.5}O_4$ has more adjunct octahedral vacancy for transition metal ions to migrate into. Therefore, the availability of adjunct

vacancies is not the limiting factor. The possibility of being limited by the size of cations can also be easily excluded because the size of Li^+ is bigger than most of transition metal ions, [51] but lithium ions can easily diffuse from one octahedral site to another octahedral site of layered oxides at the room temperature.

Therefore, it is believed that the limiting factor for the mobility of transition metal ions is their spin state, which determines their crystal field stabilization energy in the oxygen framework (Figure S2).[8] Figure 8 schematically shows a pair of adjunct octahedral sites of our interest; octahedral site shares edges with its nearest neighbors and shares face with adjunct tetrahedral sites. The migration of cations among octahedral sites is energetically preferred to take a two-step process, hopping into adjunct tetrahedral site through the sharing face before hopping into another octahedral site.[5] In general, hopping of a transition metal ion from an octahedral site into a tetrahedral site will lead to a change on the degeneracy of its d orbitals, as well as a reduction on its crystal field stabilization energy (CFSE). Thus, transition metal ions, like Mn^{4+} (d^3), Ni^{2+} (d^8), Ni^{3+} (d^7) and Ni^{4+} (d^6), are energetically preferred to stay at octahedral sites with a limited mobility owing to their high CFSE (Table S1). Therefore, there are no voltage fade phenomena in the $LiNi_{0.5}^{(2+)}Mn_{1.5}^{(4+)}O_4$, $LiNi_{0.5}^{(2+)}Mn_{0.5}^{(4+)}O_2$ and $LiNi_{1/3}^{(2+)}Co_{1/3}^{(3+)}Mn_{1/3}^{(4+)}O_2$ cathode materials during electrochemical charge/discharge cycle owing to the limited mobility of Ni^{2+}, Ni^{3+}, Ni^{4+} and Mn^{4+}. Exceptions include Mn^{2+} (d^5), generated at a very low potential, and Co^{4+} (d^5), formed at a high potential, both of which have a spherical electron distribution with a zero CFSE in both octahedral sites and tetrahedral sites (Table S1).[52-54] Hence, Mn^{2+} and Co^{4+} can have a higher mobility in oxygen framework than other transition metal ions.

Conclusion

Using $LiNi_{0.5}Mn_{1.5}O_4$ as a model material, it was confirmed that the migration of transition metal ions in the oxygen framework is possible. It is suggested that the mobility of transition metal ions in the oxygen framework is primarily determined by their spin states. Due to their high crystal field stabilization energy in oxygen framework, Mn^{4+} (d^3) and Ni^{2+} (d^8) are energetically preferred to stay in octahedral sites and have a limited mobility in $LiNi_{0.5}Mn_{1.5}O_4$. It is also predicted that Co^{4+} (d^5) and Mn^{2+} (d^5) can have a higher mobility in the oxygen framework than other cations.

Acknowledgement

Reference and Notes

1. Y. K. Sun, Z. H. Chen, H. J. Noh, D. J. Lee, H. G. Jung, Y. Ren, S. Wang, C. S. Yoon, S. T. Myung and K. Amine, *Nat. Mater.*, 2012, **11**, 942-947.
2. Y. K. Sun, S. T. Myung, B. C. Park, J. Prakash, I. Belharouak and K. Amine, *Nat. Mater.*, 2009, **8**, 320-324.
3. G. Z. Wei, X. Lu, F. S. Ke, L. Huang, J. T. Li, Z. X. Wang, Z. Y. Zhou and S. G. Sun, *Adv. Mater.*, 2010, **22**, 4364-+.
4. C. K. Lin, Y. Piao, Y. C. Kan, J. Bareno, I. Bloom, Y. Ren, K. Amine and Z. H. Chen, *ACS Appl. Mater. Interfaces*, 2014, **6**, 12692-12697.
5. K. S. Kang, Y. S. Meng, J. Breger, C. P. Grey and G. Ceder, *Science*, 2006, **311**, 977-980.

6.   J. Zheng, M. Gu, A. Genc, J. Xiao, P. Xu, X. Chen, Z. Zhu, W. Zhao, L. Pullan, C. Wang and J. G. Zhang, *Nano Lett.*, 2014, **14**, 2628-2635.

7.   C.-H. Shen, L. Huang, Z. Lin, S.-Y. Shen, Q. Wang, H. Su, F. Fu and X.-M. Zheng, *ACS Appl. Mater. Interfaces*, 2014, **6**, 13271-13279.

8.   Y. C. Kan, Y. Hu, C. K. Lin, Y. Ren, Y. K. Sun, K. Amine and Z. H. Chen, *Phys. Chem. Chem. Phys.*, 2014, **16**, 20697-20702.

9.   A. Boulineau, L. Simonin, J.-F. Colin, C. Bourbon and S. Patoux, *Nano Lett.*, 2013, **13**, 3857-3863.

10.   D. Mohanty, A. S. Sefat, J. Li, R. A. Meisner, A. J. Rondinone, E. A. Payzant, D. P. Abraham, D. L. Wood, 3rd and C. Daniel, *Phys. Chem. Chem. Phys.*, 2013, **15**, 19496-19509.

11.   D. Mohanty, A. Huq, E. A. Payzant, A. S. Sefat, J. Li, D. P. Abraham, D. L. Wood and C. Daniel, *Chem. Mater.*, 2013, **25**, 4064-4070.

12.   M. Gu, I. Belharouak, J. M. Zheng, H. M. Wu, J. Xiao, A. Genc, K. Amine, S. Thevuthasan, D. R. Baer, J. G. Zhang, N. D. Browning, J. Liu and C. M. Wang, *ACS Nano*, 2013, **7**, 760-767.

13.   M. Bettge, Y. Li, K. Gallagher, Y. Zhu, Q. Wu, W. Lu, I. Bloom and D. P. Abraham, *J. Electrochem. Soc.*, 2013, **160**, A2046-A2055.

14.   A. Ito, K. Shoda, Y. Sato, M. Hatano, H. Horie and Y. Ohsawa, *J. Power Sources*, 2011, **196**, 4785-4790.

15.   X. Ren, J. Liu and W. Zhang, *Key Engineering Mater.*, 2012, **519**. 147-151.

16.   J. H. Kim, S. T. Myung, C. S. Yoon, S. G. Kang and Y. K. Sun, *Chem. Mater.*, 2004, **16**, 906-914.

17.   Y. Shao-Horn, L. Croguennec, C. Delmas, E. C. Nelson and M. A. O'Keefe, *Nat. Mater.*, 2003, **2**, 464-467.

18.   M. S. Whittingham, *Chem. Rev.*, 2004, **104**, 4271-4301.

19.   A. R. Armstrong and P. G. Bruce, *Nature*, 1996, **381**, 499-500.

20.   J. Kim, B. H. Kim, Y. H. Baik, P. K. Chang, H. S. Park and K. Amine, *J. Power Sources*, 2006, **158**, 641-645.

21.   G. L. Xu, Y. F. Xu, J. C. Fang, F. Fu, H. Sun, L. Huang, S. H. Yang and S. G. Sun, *ACS Appl. Mater. Interfaces*, 2013, **5**, 6316-6323.

22.   Y. Ein-Eli, J. T. Vaughey, M. M. Thackeray, S. Mukerjee, X. Q. Yang and J. McBreen, *J. Electrochem. Soc.*, 1999, **146**, 908-913.

23.   S. Mukerjee, X. Q. Yang, X. Sun, S. J. Lee, J. McBreen and Y. Ein-Eli, *Mater. Res. Soc. Symp. Proc.*, 1999, **548**. 149-160.

24.   J. C. Arrebola, A. Caballero, M. Cruz, L. Hernan, J. Morales and E. R. Castellon, *Adv. Funct. Mater.*, 2006, **16**, 1904-1912.

25.   Y. L. Ding, J. A. Xie, G. S. Cao, T. J. Zhu, H. M. Yu and X. B. Zhao, *Adv. Funct. Mater.*, 2011, **21**, 348-355.

26.   J. Xiao, X. L. Chen, P. V. Sushko, M. L. Sushko, L. Kovarik, J. J. Feng, Z. Q. Deng, J. M. Zheng, G. L. Graff, Z. M. Nie, D. W. Choi, J. Liu, J. G. Zhang and M. S. Whittingham, *Adv. Mater.*, 2012, **24**, 2109-2116.

27.   J. Song, D. W. Shin, Y. H. Lu, C. D. Amos, A. Manthiram and J. B. Goodenough, *Chem. Mater.*, 2012, **24**, 3101-3109.

28. J. M. Zheng, J. Xiao, X. Q. Yu, L. Kovarik, M. Gu, F. Omenya, X. L. Chen, X. Q. Yang, J. Liu, G. L. Graff, M. S. Whittingham and J. G. Zhang, *Phys. Chem. Chem. Phys.*, 2012, **14**, 13515-13521.

29. A. Van der Ven, J. Bhattacharya and A. A. Belak, *Acc. Chem. Res.*, 2013, **46**, 1216-1225.

30. M. Sathiya, A. M. Abakumov, D. Foix, G. Rousse, K. Ramesha, M. Saubanere, M. Doublet, H. Vezin, C. P. Laisa, A. S. Prakash, D. Gonbeau, G. VanTendeloo and J. M. Tarascon, *Nat. Mater.*, 2015, **14**, 230-238.

31. J. S. Kim, C. S. Johnson and M. M. Thackeray, *Electrochem. Commun.*, 2002, **4**, 205-209.

32. M. M. Thackeray, S. H. Kang, C. S. Johnson, J. T. Vaughey and S. A. Hackney, *Electrochem. Commun.*, 2006, **8**, 1531-1538.

33. M. M. Thackeray, S.-H. Kang, C. S. Johnson, J. T. Vaughey, R. Benedek and S. A. Hackney, *J. Mater. Chem.*, 2007, **17**, 3112-3125.

34. S. H. Kang and M. M. Thackeray, *J. Electrochem. Soc.*, 2008, **155**, A269-A275.

35. J.-H. Jeong, B.-S. Jin, W.-S. Kim, G. Wang and H.-S. Kim, *J. Power Sources*, 2011, **196**, 3439-3442.

36. J. R. Croy, D. Kim, M. Balasubramanian, K. Gallagher, S.-H. Kang and M. M. Thackeray, *J. Electrochem. Soc.*, 2012, **159**, A781-A790.

37. W. C. West, J. Soler and B. V. Ratnakumar, *J. Power Sources*, 2012, **204**, 200-204.

38. H. Yu, Y. Wang, D. Asakura, E. Hosono, T. Zhang and H. Zhou, *RSC Adv.*, 2012, **2**, 8797-8807.

39. J. R. Croy, K. G. Gallagher, M. Balasubramanian, Z. Chen, Y. Ren, D. Kim, S.-H. Kang, D. W. Dees and M. M. Thackeray, *J. Phys. Chem. C*, 2013, **117**, 6525-6536.

40. X. Yang, D. Wang, R. Yu, Y. Bai, H. Shu, L. Ge, H. Guo, Q. Wei, L. Liu and X. Wang, *J. Mater. Chem. A*, 2014, **2**, 3899-3911.

41. A. Vu, L. K. Walker, J. Bareño, A. K. Burrell and I. Bloom, *J. Power Sources*, 2015, **280**, 155-158.

42. F. Fu, G. L. Xu, Q. Wang, Y. P. Deng, X. Li, J. T. Li, L. Huang and S. G. Sun, *J. Mater. Chem. A*, 2013, **1**, 3860-3864.

43. H. Deng, I. Belharouak, Y.-K. Sun and K. Amine, *J. Mater. Chem.*, 2009, **19**, 4510.

44. Z. H. Chen, Y. Ren, Y. Qin, H. M. Wu, S. Q. Ma, J. G. Ren, X. M. He, Y. K. Sun and K. Amine, *J. Mater. Chem.*, 2011, **21**, 5604-5609.

45. K. An, H. D. Skorpenske, A. D. Stocia, D. Ma, X. L. Wang and E. Cakmak, Metall. Mater. Trans. A, 2011, 42, 95–99.

46. L. Cau, Z. C. Liu, A. Ke and Liang, C. D., *J. Mater. Chem. A*, 2013, **1**, 6908.

47. D. Pasero, N. Reeves, V. Prolong and A. R. West, *J. Electrochem. Soc.*, 2008, 4, A282-A291.

48. L. P. Wang, H. Li, X. J. Huang and E. Baudrin, *Solid State Ionics*, 2011, **193**, 32–38.

49. S. Kim, X. H. Ma, S. P. Ong and G. Ceder, *Phys. Chem. Chem. Phys.*, 2012, **14**, 15571-15578.

50.   Y. S. Meng and M. Elena Arroyo-de Dompablo, *Acc. Chem. Res.*, 2013, **46**, 1171-1180.
51.   R. D. Shannon, *Acta Cryst. A*, 1976, **32**, 751-767.
52.   J. D. Dunitz and L. E. Orgel, *J. Phys. Chem. Solids*, 1957, **3**, 318-323.
53.   J. D. Dunitz and L. E. Orgel, *J. Phys. Chem. Solids*, 1957, **3**, 20-29.
54.   D. S. McClure, *J. Phys. Chem. Solids*, 1957, **3**, 311-317.
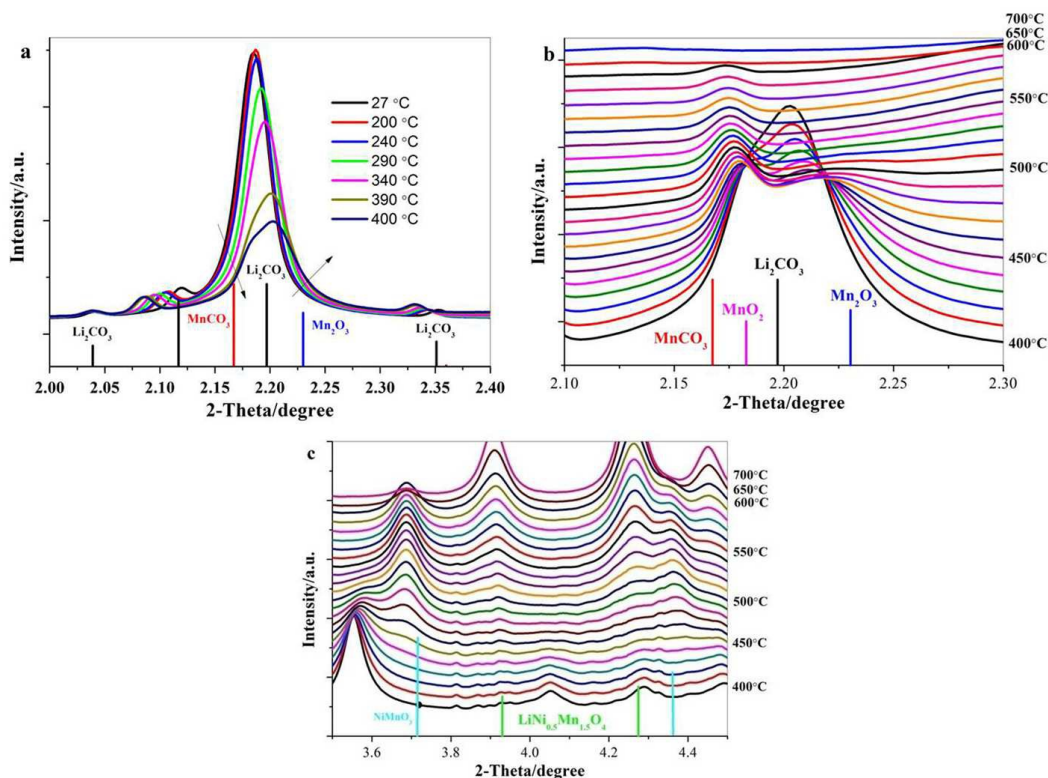
Supporting Information

Figure S1 (a) HEXRD patterns collected at various temperature with a 2θ region of 2.00-2.40°, (b) HEXRD patterns collected from 400 °C to 700 °C within a 2θ region of (b) 2.10-2.30° and (c) 3.5-4.5°.
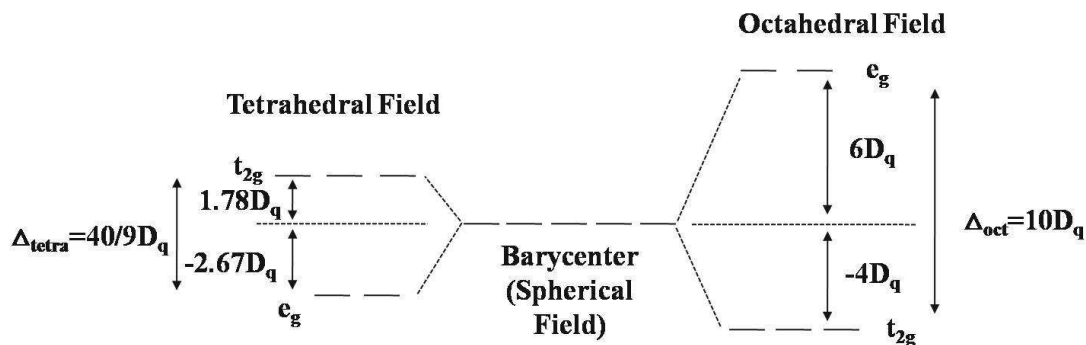
Figure S2 Crystal field stabilization energy for octahedral and tetrahedral field.

Table S1 Configuration and Stabilization energy for transition metal ions in crystal fields

		Octahedral		Tetrahedral	
Cation	Number of d electrons	Configuration	Stabilization energy	Configuration	stabilization energy
Ni^{2+}	8	$(t_{2g})^6(e_g)^2$	$-12D_q$	$(e_g)^4(t_{2g})^4$	$-3.56D_q$
Ni^{3+}	7	$(t_{2g})^5(e_g)^2$	$-8D_q$	$(e_g)^4(t_{2g})^3$	$-5.34D_q$
Ni^{4+}	6	$(t_{2g})^4(e_g)^2$	$-4D_q$	$(e_g)^3(t_{2g})^3$	$-2.67D_q$
Mn^{4+}	3	$(t_{2g})^3(e_g)^0$	$-12D_q$	$(e_g)^2(t_{2g})^1$	$-3.56D_q$
Mn^{2+}	5	$(t_{2g})^3(e_g)^2$	0	$(e_g)^2(t_{2g})^3$	0
Co^{4+}	5	$(t_{2g})^3(e_g)^2$	0	$(e_g)^2(t_{2g})^3$	0

In octahedral field, the energy gap ($\triangle$oct) is referred to as $10D_q$, the crystal field splitting energy. And the crystal field stabilization energy (CFSE) is the stability that results from placing a transition metal ion in the crystal field generated by a set of ligands. In an octahedral case, the t_{2g} set becomes lower in energy than the orbitals in the barycenter. As a result of this, if there are any electrons occupying these orbitals, the metal ion is more stable in the ligand field relative to the barycenter by an amount known as the CFSE. Conversely, the e_g orbitals (in the octahedral case) are higher in energy than in the barycenter, so putting electrons in these reduces the amount of CFSE. Therefore, the total CFSE of transition metal ions equal to the sum of the d electron number in the t_{2g} orbital and e_g orbital multiply by their energy. The case of tetrahedral filed is similar to the octahedral fields except the impact of e_g and t_{2g} on CFSE is reverse and the splitting energy of tetrahedral fields is only 4/9 of the octahedral fields.

For example, Ni^{2+}, $CFSE_{oct}=2\times (6Dq) + 6\times (-4Dq) = -12D_q$

$CFSE_{tetra}=4\times 1.78Dq + 4\times (-2.67Dq) = -3.56D_q$

Table of Contents
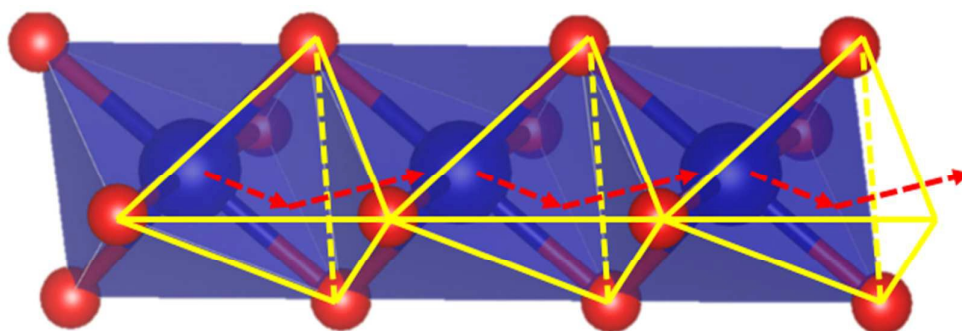
In situ high-energy X-ray diffraction and neutron diffraction were deployed to trace the

migration of transition metal ions in $LiNi_{0.5}Mn_{1.5}O_4$.